Journal of Magnetic Resonance **145,** 357–363 (2000)
doi:10.1006/jmre.2000.2100, available online at http://www.idealibrary.com on IDEAL®

ESEEM Measurements with Time-Resolved Detection of the Entire ESE Signal Shape

Andrei V. Astashkin,[1,2] Valeri V. Kozlyuk, and Arnold M. Raitsimring

Department of Chemistry, University of Arizona, Tucson, Arizona 85721-0041

Received February 4, 2000

In this work we discuss the extension of electron spin-echo envelope modulation (ESEEM) measurements to the additional time dimension, the spin-echo coordinate. The time-resolved acquisition of the entire spin-echo signal shape retains information on the dependence of the ESEEM amplitude on the position within the ESE signal. Therefore, not only can such acquisition be completely substituted for the boxcar integration in ESEEM measurements, but it can also improve the performance of the ESEEM experiments in terms of obtaining correct modulation amplitudes and a better signal/noise ratio. Implementing such an acquisition in pulse-adjustable ESEEM measurements transforms these techniques into routine and convenient experiments used to increase the modulation amplitude.

Key Words: **ESE; ESEEM; SECSY; data acquisition; signal-to-noise ratio.**

INTRODUCTION

There are several approaches to improving performance in electron spin-echo envelope modulation (ESEEM) measurements. Some of them, including the reduction of spectrometer dead time and an increase in the spectral coverage of microwave (mw) pulses, have seen much progress during the past decade, owing to the development of fast mw switches, resonators with high filling and low quality factors, low-noise amplifiers, etc. (*1–4*). Improvements in the data acquisition system also hold a potential to enhance the quality of the ESEEM data. This approach, however, has not been extensively explored because, until recently, data acquisition has mostly remained in a state of 30 years' antiquity and was based on gated boxcar integration.

Because the phase of the ESEEM harmonics varies across the ESE signal (which fact constitutes the background for spin-echo correlation spectroscopy, SECSY (*5, 6*)), in a conventional ESEEM experiment, the width of the boxcar gate should be minimized to avoid distortions of the modulation amplitude. At the same time, the gate width should be large enough to provide a reasonable signal/noise (S/N) ratio for a given signal. Such requirements may be mutually exclusive for a boxcar, but they can easily be fulfilled if the entire ESE signal shape is digitized and stored in the experiment. However, until recently it was impossible to obtain commercial hardware, namely fast data acquisition (DAQ) boards or digital oscilloscopes, with adequate signal processing parameters. The existing DAQ boards for personal computers suffered from low time resolution and the digital oscilloscopes, while exhibiting a satisfactory time resolution, suffered from a slow data transfer rate to the computer.

The situation started to change about 3 years ago, when Bruker implemented the fast transient signal averager "SpecJet" in their new E580 series of pulsed EPR spectrometers, and Gage Applied Sciences, Inc., made the first commercial 500-MHz DAQ boards for personal computers (PC). Employing such data acquisition devices adds an extra time dimension to any ESEEM experiment, but does not increase the duration of the experiment because of adequate sampling and retriggering rates. Appropriate mathematical processing of the acquired ESE shapes yields a modulation amplitude without phase distortion and an optimized S/N ratio for a given experiment.

Here we report our first results on optimizing data acquisition in some ESEEM experiments. We also demonstrate that acquisition of the entire ESE signal in pulse-adjustable and pulse-matching ESEEM experiments (*7–9*) eliminates a tiresome and time-consuming procedure of searching for the maximal modulation amplitude over the spin-echo coordinate, thus simplifying these experiments and transforming them into routine techniques.

EXPERIMENTAL

In our experiments two samples have been used. The first one was a glassy toluene solution (1 mM) of 2,2,6,6-tetramethyl-1-piperidinyloxy (TEMPO) stable free radical obtained from Aldrich. The second sample was *cis*,*trans*-(L-N_2S_2)$Mo^{V}O(SCH_2Ph)$, L-Mo^{V} (*10*), in 1:1 $C_2Cl_2D_4$:dimethylformamide-d_7 solution (2 mM). The experiments have been performed on homebuilt broadband pulsed EPR spectrometers operating at mw frequencies ranging from 2 to 8 (*11*) and from 8 to 18 GHz (*12*). The measurement temperature was 20 K.

The ESE transients have been recorded with fast DAQ

[1] On leave from the Institute of Chemical Kinetics and Combustion, 630090 Novosibirsk, Russia.

[2] To whom correspondence should be addressed. Fax: (520) 621-8407. E-mail: andrei@u.arizona.edu.

1090-7807/00 $35.00

boards (CS8500, from Gage Applied Sciences, Inc.; 2 ns time resolution, 8 bit amplitude resolution, and >200 MHz bandwidth; see www.gage-applied.com for more details). After every pulse shot, the data recorded in the memory of the DAQ boards were transferred into the PC memory via the PCI bus. With these DAQ boards, data transfer rates of up to 15 kHz were possible. The experiments, however, were performed with a pulse repetition rate of 500 Hz only, which was limited by the saturation of the TEMPO and L-Mo^{V} ESE signals at the measurement temperature.

RESULTS AND DISCUSSION

Consider an acquisition system with integration of the ESEEM signal in the time window Δt_I. The ESEEM signal $V(t)$ produced by the nonideal mw pulses with optimal nominal flip angles often has a nearly Gaussian shape,

$$V(t) = V_0 \exp(-2t^2/\delta^2), \qquad [1]$$

where δ is the width of the ESE signal between the maximum slope points and the time origin is placed in the center of the ESE signal. V_0 is the amplitude of the ESE signal. If the integration gate is situated symmetrically with respect to the signal center, the total integrated signal is

$$V_I(\Delta t_I) = \sqrt{\frac{\pi}{2}}\, V_0 \delta \cdot \mathrm{erf}\left(\frac{\Delta t_I}{\sqrt{2}\,\delta}\right). \qquad [2]$$

In a real experiment some amount of noise is superimposed on the signal. The noise contribution into the total integral is proportional to $\Delta t_I^{1/2}$ (at least, if the maximum frequency in the noise bandwidth is greater than $1/\Delta t_I$). The S/N ratio is thus proportional to

$$R(\Delta t_I) \propto \frac{1}{\sqrt{\Delta t_I}}\, \mathrm{erf}\left(\frac{\Delta t_I}{\sqrt{2}\delta}\right) \qquad [3]$$

and has a maximum at $\Delta t_I = \sqrt{2}\,\delta$. This integration interval optimizes the S/N ratio for the ESE signal. However, as we have already mentioned in the Introduction, the phase of the ESEEM harmonics varies across the ESE signal. Therefore, the integration gate that optimizes the S/N ratio for the ESE signal is not necessarily optimal for the S/N ratio with respect to the ESEEM.

The optimization of the S/N ratio without loss of modulation amplitude due to phase distortions is most clearly demonstrated for the primary ESEEM. In the case of complete excitation of the ESEEM, the primary ESE amplitude is described by the expression (*5*)

$$V(\tau, t) = G(t) \cdot f(\tau, t), \qquad [4]$$

where $G(t)$ is the shape of the spin-echo signal, $f(\tau, t)$ is the ESEEM, and the time variables τ and t denote the time interval between the mw pulses and the time shift from the ESE maximum (located at time τ after the second pulse), respectively. Below, the time variable t is referred to as the spin-echo coordinate.

The ESE signal shape is explicitly expressed as (*13*)

$$G(t) = \int_{-\infty}^{\infty} \alpha_1^* \beta_1^* (\beta_2^*)^2 g(\Delta\omega) \exp(-i\Delta\omega t)\, d(\Delta\omega)$$

$$\alpha_k = \cos\left(\frac{\omega_{Nk} t_{pk}}{2}\right) - i\, \cos(\varphi_k) \sin\left(\frac{\omega_{Nk} t_{pk}}{2}\right);$$

$$\beta_k = -i\, \sin(\varphi_k) \sin\left(\frac{\omega_{Nk} t_{pk}}{2}\right)$$

$$\omega_{Nk} = \sqrt{\omega_{1k}^2 + \Delta\omega^2}; \quad \varphi_k = \mathrm{atan}\left(\frac{\omega_{1k}}{\Delta\omega}\right), \qquad [5]$$

where ω_{1k} is the amplitude of the kth mw pulse and t_{pk} is the kth pulse duration, $\Delta\omega$ is the frequency offset from resonance, and $g(\Delta\omega)$ is the shape of the EPR spectrum due to all factors but the interaction with the nucleus responsible for the ESEEM.

The ESEEM term is given by (*5*, *6*)

$$f(\tau, t) = \left(\frac{1 + \sqrt{1-k}}{2}\right)^2 c_{\delta'} + \left(\frac{1 - \sqrt{1-k}}{2}\right)^2 c_{\sigma'} + \frac{k}{4}\left[c_{\alpha+\delta'} + c_{\alpha+\sigma'} + c_{\beta-\delta'} + c_{\beta+\sigma'} - c_{\delta+\delta'} - c_{\sigma+\sigma'}\right] \qquad [6]$$

or, in a slightly different form,

$$f(\tau, t) = \left(\frac{1 + \sqrt{1-k}}{2}\right)^2 c_{\delta'} + \left(\frac{1 - \sqrt{1-k}}{2}\right)^2 c_{\sigma'} + \frac{k}{4}\left[2c_{\beta'}c_{\alpha+\alpha'} + 2c_{\alpha'}c_{\beta+\beta'} - c_{\delta+\delta'} - c_{\sigma+\sigma'}\right]. \qquad [7]$$

In Eqs. [6] and [7], c stand for cosine functions and the subscripts α, β, σ, δ, α', β', σ' and δ' denote the arguments of the cosines $2\pi\nu_\alpha\tau$, $2\pi\nu_\beta\tau$, $2\pi\nu_\sigma\tau$, $2\pi\nu_\delta\tau$, $\pi\nu_\alpha t$, $\pi\nu_\beta t$, $\pi\nu_\sigma t$, and $\pi\nu_\delta t$, respectively (primed arguments correspond to

halved frequencies). The nuclear transition frequencies at α and β electron spin manifolds are

$$\nu_\alpha = \sqrt{\frac{T_{ZX}^2 + T_{ZY}^2}{4} + \left(\nu_I - \frac{a_{iso} + T_{ZZ}}{2}\right)^2};$$
$$\nu_\beta = \sqrt{\frac{T_{ZX}^2 + T_{ZY}^2}{4} + \left(\nu_I + \frac{a_{iso} + T_{ZZ}}{2}\right)^2}, \qquad [8]$$

where ν_I is a nuclear Zeeman frequency, a_{iso} is an isotropic hyperfine interaction (hfi) constant, and T_{ij} are the components of the anisotropic hfi tensor. $\nu_\sigma = \nu_\alpha + \nu_\beta$ and $\nu_\delta = \nu_\alpha - \nu_\beta$ are the sum and difference combination frequencies. The modulation amplitude factor k is (*14*)

$$k = \frac{\nu_I^2(T_{ZX}^2 + T_{ZY}^2)}{\nu_\alpha^2 \nu_\beta^2}. \qquad [9]$$

Equations [4]–[7] describe correlated two-dimensional (2D) oscillations of the primary ESE signal in τ and t dimensions. The oscillations in the τ manifold have the frequencies of the nuclear transitions ν_α and ν_β and their linear combinations ν_σ and ν_δ. The oscillations along t have the frequencies of the EPR transitions $\Delta\omega/2\pi \pm \nu_\delta/2$ and $\Delta\omega/2\pi \pm \nu_\sigma/2$. If the hfi substantially exceeds inhomogeneous broadening (e.g., a single crystal), $g(\Delta\omega)$ in Eq. [5] may be approximated by the δ function, and a 2D Fourier transform (FT) of $V(\tau, t)$ results in a resolved SECSY spectrum, $V(\nu, \nu')$, showing correlations between the nuclear modulation frequencies (ν) and the frequencies of EPR transitions (ν'). Examples of such spectra can be found elsewhere (*5*, *6*, *15*).

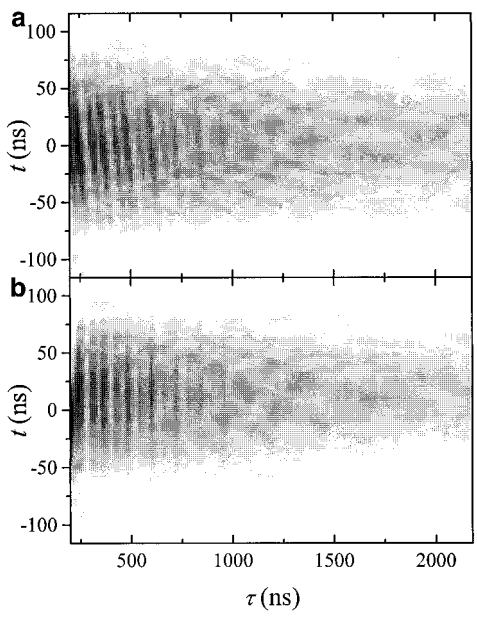

FIG. 1. (a) The experimental dependence of the primary ESE signal shape on τ for the glassy toluene solution of TEMPO. (b) Same as (a), but after signal phasing as explained in the text. Experimental conditions: $\nu_{mw} = 5.483$ GHz, $B_0 = 195.3$ mT (corresponding to the maximum of the EPR spectrum), and the mw pulse durations are 30 and 60 ns (providing the nominal flip angles of 90° and 180°, respectively).

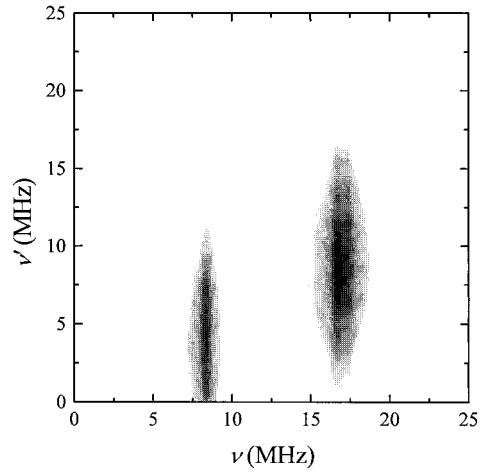

FIG. 2. The (++) quadrant of the 2D amplitude FT spectrum of the ESEEM data shown in Fig. 1a. The horizontal axis (ν) corresponds to the FT along τ. The vertical axis (ν') corresponds to the FT along t. Before the FT along τ, the nonoscillating component (approximated by the smoothing cubic spline) was subtracted from the ESE decays. No apodization has been used. This is, actually, the SECSY spectrum with removed autocorrelation peaks at $\nu = 0$.

For orientationally disordered samples, the characteristic width of $g(\Delta\omega)$ usually substantially exceeds hfi parameters and nuclear Zeeman frequency, which results in smearing of the (ν, ν') correlation lines along ν'. For a case of weak hfi ($|a_{iso} + T_{ZZ}| < 2\nu_I$ and, thus, $\nu_\alpha \approx \nu_\beta \approx \nu_I$) the (α, σ'), (β, σ'), (α, δ'), and (β, δ') correlation peaks will be extended along ν' between 0 ($\approx\nu_\delta/2$) and ν_I ($\approx\nu_\sigma/2$), with a center located at $(\nu_I, \nu_I/2)$, and the (σ, σ') correlations will be centered at $(2\nu_I, \nu_I)$.

The described features of the primary ESEEM are demonstrated using the TEMPO radical in a glassy toluene solution. The 2D time domain data, $V(\tau, t)$, are presented in Fig. 1a. The ESEEM in Fig. 1a manifests itself as a series of ridges and troughs that are not perpendicular to the τ axis because the phases of the oscillations in the τ manifold linearly depend on t and vice versa (see Eqs. [6] and [7]). The 2D FT spectrum of this ESEEM is presented in Fig. 2. It shows two prominent features at frequencies of (8.3, 4.1) MHz and (16.6, 8.3) MHz, both of which are extended along ν'. The former peak is assigned to the (α, σ'), (β, σ'), (α, δ'), and (β, δ') correlations and, in agreement with the above theoretical considerations, is located at $(\nu_I, \nu_I/2)$. The latter peak is assigned to the (σ, σ') correlations and is located at $(2\nu_I, \nu_I)$. This peak shows a doublet splitting along the ν axis, with the lower-frequency component of the doublet associated with the distant matrix protons and the higher-frequency component arising from the methyl protons of the TEMPO radical (*16*).

Figure 3a depicts the shape of the primary ESE signal

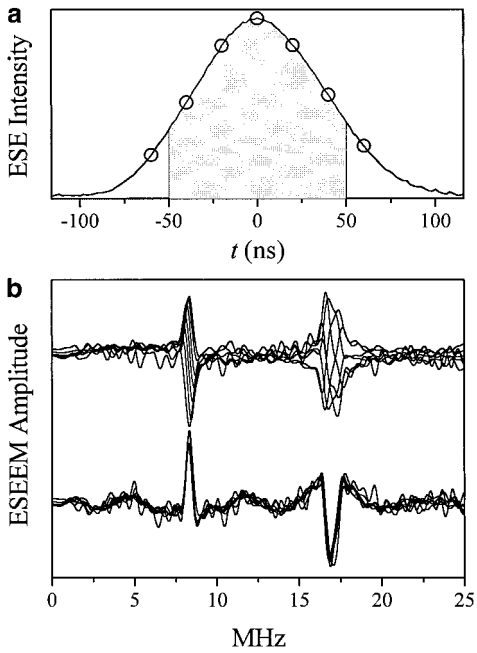

FIG. 3. (a) The shape of the primary ESE signal obtained from the data presented in Fig. 1a by integration over τ. The shaded area corresponds to the S/N optimal integration limits. (b) Upper group of traces: Superimposed cosine FT spectra corresponding to the positions in the ESE signal marked by open circles in (a). Lower group of traces: The same, but after the appropriate linear phase correction. Before the FT, the ESEEM traces were normalized by the ESE signal decay along τ and the nonoscillating component has been subtracted. To suppress the effects due to the data truncation at τ_{max} (where τ_{max} is the maximal τ in the data set), the cosine half-bell window (defined as $W(\tau) = 1$ at $\tau < \tau_{max}/2$, and $W(\tau) = [1\text{-}\cos(2\pi(\tau_{max} - \tau)/\tau_{max})]/2$ at $\tau_{max}/2 \leq \tau \leq \tau_{max}$) has been applied. Therefore, the resolution of the sum combination line in these spectra is noticeably worse than that in the 2D spectrum shown Fig. 2.

obtained from the data presented in Fig. 1a by integration over τ. Figure 3b shows the cosine FT spectra corresponding to the positions in the ESE signal marked by open circles in Fig. 3a. The upper group of traces in Fig. 3b represents superimposed spectra of the normalized (by the signal decay along τ) ESEEMs with the phases determined by the spin-echo coordinates t. One can see that the dependence of the ESEEM phase on t is quite appreciable and makes up about π for the ν_I harmonic and about 2π for the $2\nu_I$ harmonic in the range of t presented. Therefore, integration of the ESE signal (Fig. 1a) in broad limits will result in a decrease in the observed modulation amplitude. In particular, it may prove impossible to obtain correct modulation amplitudes for the boxcar gate width optimizing the S/N ratio for the ESE signal.

As an example, trace 1 in Fig. 4 shows the ESEEM spectrum corresponding to the center of the ESE signal presented in Figs. 1a and 3a. Trace 2 in the same figure is obtained by integration of the ESE signal in the limits shown in Fig. 3a by shading and corresponding to the expected optimal S/N ratio ($\Delta t_I = \sqrt{2}\,\delta \approx 100$ ns for this ESE signal). One can see that the integration of the ESE signal leads to the decrease in the amplitude of the spectrum lines. In this particular experiment the optimal integration resulted in about a 20% decrease in the fundamental proton line at ν_I and in almost a fourfold decrease in the sum combination line at $2\nu_I$. In order to show that this decrease is not related to the variations of the ESEEM amplitude across the ESE signal (which, in principle, is conceivable for the incomplete excitation of the EPR spectrum by mw pulses), the lower group of traces in Fig. 3b presents the superimposed spectra of the normalized ESEEM (same as the upper group of traces) after linear phase correction. One can see that, apart from the noise-induced changes, the amplitudes of the lines in these spectra are practically identical; i.e., the modulation amplitude is proportional to the spin-echo amplitude.

Depending on the parameters of the mw pulses used in experiment, the decrease in the ESEEM amplitude caused by the signal integration can be smaller or greater than that demonstrated in Fig. 4. In general, however, this decrease is unavoidable as long as the detection is performed using a boxcar integrator. For instance, quantitatively the same effects will be observed in the X-band primary ESEEM experiment employing mw pulses of about 16 and 32 ns long.

With the whole ESE shape dependence on τ at hand, however, the problem can easily be solved using, e.g., a phase correction achieved by shifting every slice of the experimental 2D data at a given t by $-t/2$ along τ. This procedure completely eliminates the phase dependence of combination harmonics on t and considerably reduces the phase variation of the

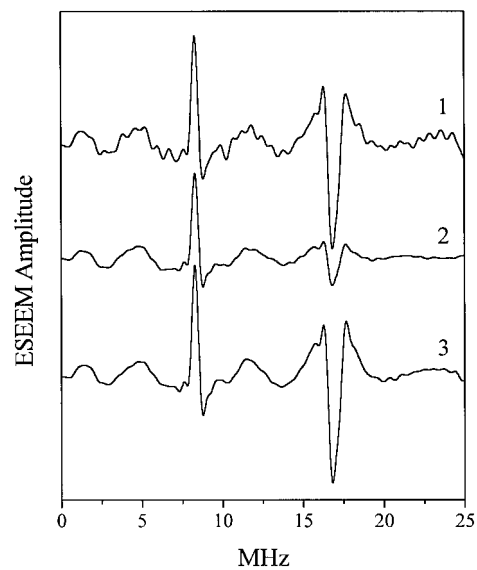

FIG. 4. Trace 1: The cosine FT spectrum of the primary ESEEM corresponding to the center of the ESE signal shown in Figs. 1a and 3a. Trace 2: The cosine FT spectrum of the ESEEM shown in Fig. 1a, integrated within the limits shown by shading in Fig. 3a. Trace 3: The cosine FT spectrum of the phased ESEEM shown in Fig. 1b, integrated within the limits shown by shading in Fig. 3a. Before the FT, the (integrated) ESEEM traces were normalized by the ESE signal decay along τ and a window function has been applied as described in the legend to Fig. 3b.

fundamental harmonics. Indeed, after such shifting, Eq. [7] gives

$$f(\tau, t) = \left(\frac{1 + \sqrt{1-k}}{2}\right)^2 c_{\delta'} + \left(\frac{1 - \sqrt{1-k}}{2}\right)^2 c_{\sigma'} + \frac{k}{4}[2c_{\beta'}c_{\alpha} + 2c_{\alpha'}c_{\beta} - c_{\delta} - c_{\sigma}], \qquad [10]$$

where the ν_σ and ν_δ harmonics do not contain the phase dependence on t anymore.

The application of such a phase correction to our experimental data is shown in Fig. 1b. One can see that after the correction the modulation ridges are perpendicular to the τ axis, allowing the integration of the ESEEM over the ESE signal almost without loss of the modulation amplitude. Indeed, the amplitudes of the lines in the ESEEM spectrum obtained by integration of the phase-corrected ESE signal in the S/N optimal limits (trace 3 in Fig. 4) are similar to those in the spectrum obtained by FT of the slice corresponding to the ESE maximum (trace 1 in Fig. 4). At the same time, the noise level in trace 3 is considerably lower than that in trace 1 and is similar to that in trace 2. Thus, the phasing of the ESEEMs corresponding to different points of the ESE signal allows one to considerably improve the S/N ratio without distortion of the line intensities in the primary ESEEM spectra.

Another way to use the ESE shape (if one is not interested in the phases of the ESEEM harmonics) may be the summation of the magnitude FTs for every τ slice in optimal limits over the spin-echo coordinate. Such method may be applied, for example, to the stimulated ESEEM, where the phase dependence on the spin-echo coordinate is more complicated (*5*)

$$f(\tau, t, T) = \left(\frac{1 + \sqrt{1-k}}{2}\right)^2 c_{\delta'} + \left(\frac{1 - \sqrt{1-k}}{2}\right)^2 c_{\sigma'} + \frac{k}{4}[c_{\beta'}c_{\alpha+\alpha'} + (c_{\beta'} + c_{\beta+\beta'})c_{\alpha+\bar{\alpha}+\alpha'} + c_{\alpha'}c_{\beta+\beta'} + (c_{\alpha'} + c_{\alpha+\alpha'})c_{\beta+\bar{\beta}+\beta'}] \qquad [11]$$

and cannot be eliminated completely by shifting the τ or T slices by $-t/2$. More sophisticated methods of processing 3D data (with one of the dimensions being the spin-echo coordinate), based on integral properties of the spin-echo signal, will be discussed in a future publication in connection with the separation of four-pulse and stimulated ESEEMs in a hyperfine sublevel correlation (HYSCORE) experiment.

To conclude this section, we should mention a low-pass filtering of the ESE signal, which is another popular technique for reducing the noise contribution to the ESEEM. The frequency filtering is equivalent to the convolution of the unfiltered signal shape with the time domain Fourier image of the amplitude-frequency characteristic of the filter. For the rectangular low-pass filter with a cutoff frequency of ν_c this function is $\sin(\nu_c t)/t$, and thus

$$V_F(\tau, t) = \int_{-\infty}^{\infty} V(\tau, t + \tilde{t}) \frac{\sin \nu_c \tilde{t}}{\tilde{t}} d\tilde{t}, \qquad [12]$$

where $V_F(\tau, t)$ is the filtered ESE shape. For the point corresponding to the maximum of the ESE signal ($t = 0$), the convolution reduces to the weighted integration over the ESE shape:

$$V_F(\tau, 0) = \int_{-\infty}^{\infty} V(\tau, \tilde{t}) \frac{\sin \nu_c \tilde{t}}{\tilde{t}} d\tilde{t}. \qquad [13]$$

The main lobe of the function $\sin(\nu_c t)/t$ has a half-height width of about $1/(2\nu_c)$ and the low-pass filtering is thus practically similar to the use of a boxcar integrator with the equivalent integration gate width equal to $1/(2\nu_c)$, which will lead to a distortion of the modulation amplitude similar to that discussed above.

Different reasons for digitizing the entire spin-echo shape

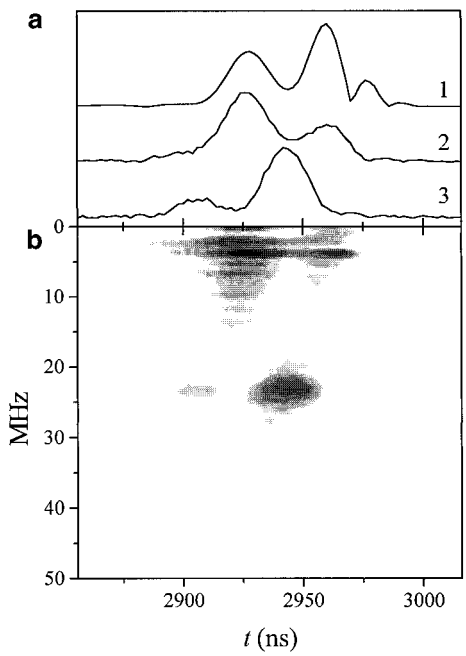

FIG. 5. (b) The 2D (frequency–spin-echo coordinate) representation of the amplitude FT spectrum of the "2 + 1" ESEEM of L-Mo^{V}. (a) Trace 1: The modulus of the ESE shape integrated over τ' (the interval between the first and second mw pulses). Trace 2: The projection of the ^{2}H ESEEM spectrum line at 3.6 MHz (see (b)). Trace 3: The projection of the ^{1}H ESEEM spectrum line at 23.3 MHz (see (b)). Experimental conditions: ν_{mw} = 15.066 GHz, B_0 = 548.14 mT (corresponding to the maximum of the EPR spectrum), and the mw pulse durations are 12 ns (~90°), 50 ns (~360°), and 12 ns (~90°).

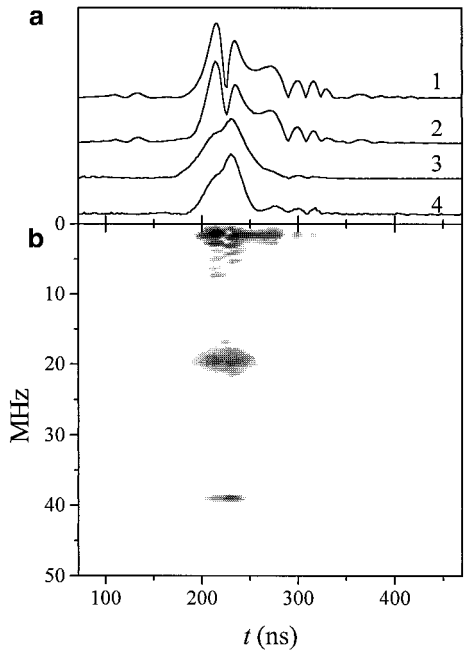

FIG. 6. (b) The 2D (frequency–spin-echo coordinate) representation of the amplitude FT spectrum of the pulse-matched primary ESEEM of L-Mo^{V}. (a) Trace 1: The modulus of the ESE shape integrated over τ. Trace 2: The projection of the ^{14}N ESEEM spectrum line at 1.95 MHz (see (b)). Trace 3: The projection of the ^{1}H Zeeman spectrum line at 23.3 MHz (see (b)). Trace 4: The projection of the ^{1}H double Zeeman spectrum line at 46.7 MHz (see (b)). Experimental conditions: ν_{mw} = 15.066 GHz, B_0 = 548.14 mT (corresponding to the maximum of the EPR spectrum), and the durations of both mw pulses are 120 ns (~720°).

become apparent, if we consider the pulse-adjustable techniques ("2 + 1" (*7*), "1 + 2" (*8*), pulse-matched ESEEM (*9*)). A characteristic feature of these techniques is the use of mw pulses with high turning angles (usually, more than 2π), and the amplitudes adjusted to match the electron nutation and nuclear transition frequencies. Such mw pulses are usually tens to hundreds of nanoseconds long, and the spin-echo signal they form has a similar duration. The spin-echo and modulation amplitudes in these methods are not factorized as in usual ESEEM techniques employing hard and short mw pulses. The maxima of spin-echo signals do not correspond to those of the modulation amplitude, and the positions of the latter are known only in cases of extremely weak hyperfine interaction (*17*). This circumstance makes the use of these techniques very inconvenient in an experiment with the boxcar integrator-based acquisition system. Due to this inconvenience, and despite the fact that these techniques may give a huge increase in modulation amplitude (as compared to the usual two- and three-pulse methods), they were never actively used in practice.

With digitizing the entire spin-echo signal, the pulse-adjustable techniques can be used as effectively as any conventional method. As an example, Fig. 5b shows the dependence of the "2 + 1" ESEEM spectrum of L-Mo^{V} on the spin-echo coordinate. The spectrum exhibits a line at 23.3 MHz due to the weakly coupled ligand protons. The low-frequency lines are contributed by solution deuterons (at 3.6 MHz) and ligand nitrogens. Traces 2 and 3 in Fig. 5a show, respectively, the variations of the deuteron and proton line amplitudes along the spin-echo coordinate. Trace 1 in the same figure shows the absolute value of the ESE signal shape. One can see that the maxima of different modulation harmonics appear at different places in the ESE signal and the modulation amplitude is not proportional to the ESE signal amplitude. Actually, in this particular case the *maximum* of the proton modulation corresponds to the *minimum* of the spin-echo signal. Similar data are presented in Fig. 6 for the primary ESEEM with matched mw pulses, demonstrating the same feature as "2 + 1" ESEEM. From Figs. 5 and 6 one can see that with the acquisition of the entire ESE signal shape, the tiresome procedure of searching for the maximum of the modulation amplitude within the time span of the ESE signal (by readjusting the boxcar gate position) is eliminated.

CONCLUSION

In this work we have demonstrated that the currently available commercial fast signal-digitizing boards can be completely substituted for gated acquisition and can be used in everyday ESEEM measurements for obtaining quantitative information on modulation amplitude and improving the *S*/*N* ratio in ESEEM measurements. Implementing such acquisition devices converts pulse-adjustable ESEEM techniques into routine and convenient experiments used for increasing the modulation amplitude.

ACKNOWLEDGMENTS

The financial support of NSF DBI-9604939 (to Drs. A. Raitsimring and F. A. Walker) for construction of the pulsed EPR spectrometer is gratefully acknowledged. Dr. A. Astashkin is thankful to NIH DK 31038 (to Dr. F. A. Walker) for financial support of the research presented herein.

REFERENCES

1. P. P. Borbat, R. H. Crepeau, and J. H. Freed, *J. Magn. Reson.* **127,** 155 (1997).
2. J. Forrer, S. Pfenninger, G. Sierra, G. Jeschke, A. Schweiger, B. Wagner, and Th. Weiland, *Appl. Magn. Reson.* **10,** 263 (1996).
3. G. A. Rinard, R. W. Quine, R. Song, G. R. Eaton, and S. S. Eaton, *J. Magn. Reson.* **140,** 69 (1999).
4. G. A. Rinard, R. W. Quine, J. R. Harbridge, R. Song, G. R. Eaton, and S. S. Eaton, *J. Magn. Reson.* **140,** 218 (1999).
5. D. Gamliel and J. H. Freed, *J. Magn. Reson.* **89,** 60 (1990).
6. S. Lee, B. R. Patial, and J. H. Freed, *J. Chem. Phys.* **98,** 3665 (1993).
7. V. V. Kurshev, A. V. Astashkin, and A. M. Raitsimring, *J. Struct. Chem.* **29,** 62 (1988).

8. P. P. Borbat and A. M. Raitsimring, *J. Magn. Reson. A* **114,** 261 (1995).

9. G. Jeschke, R. Rakhmatullin, and A. Schweiger, *J. Magn. Reson.* **131,** 261 (1998).

10. M. L. Mader, M. D. Carducci, and J. H. Enemark, *Inorg. Chem.* **39,** 525 (2000).

11. A. V. Astashkin, V. Kozlyuk, and A. M. Raitsimring, Abstracts of the 40th Rocky Mountain Conference on Analytical Chemistry, Denver, CO, July 26–30 (1998), additional materials.

12. P. P. Borbat and A. M. Raitsimring, Abstracts of the 36th Rocky Mountain Conference on Analytical Chemistry, Denver, CO, p. 94, July 31–August 5 (1994).

13. A. Bloom, *Phys. Rev.* **98,** 1105 (1955).

14. W. B. Mims, *Phys. Rev. B* **5,** 2409 (1972).

15. A. M. Raitsimring, D. H. Crepeau, and J. H. Freed, *J. Chem. Phys.* **102,** 8746 (1995).

16. A. V. Astashkin and A. M. Raitsimring, *J. Magn. Reson.* **143,** 280 (2000).

17. A. Raitsimring and P. Borbat, *Chem. Phys. Lett.* **262,** 8 (1996).